Journal Name

ARTICLE

Kinetically Controlled Redox Behaviors of $K_{0.3}MnO_2$ Electrodes for High Performance Sodium-Ion Batteries

Jiasheng Qian, Ying San Chui, Guijun Li, Mei Lin, Chi Man Luk, Chun Hin Mak, Biao Zhang, Feng Yan and Shu Ping Lau*

Due to its abundance, high theoretical capacity, and environmental compatibility, manganese dioxide (MnO_2) is regarded as a potential electrode material for sodium-ion batteries. Nevertheless, the severe side reactions including manganese dissolution and Mn^{3+} disproportionation reaction are common challenges to the manganese-based electrodes that causes a huge capacity fade, further limiting their practical applications. To address the issues, here the environmental friendly K-birnessite MnO_2 ($K_{0.3}MnO_2$) nanosheets are directly inkjet-printed on the stainless steel sheet to serve as the electrode, while the diglyme-based electrolyte is used to fabricate a sodium-ion battery. In contrast to the conventional two-step redox reactions involving $Mn^{4+}/Mn^{3+}/Mn^{2+}$ couples, the as-printed $K_{0.3}MnO_2$ electrode shows enhanced redox activity of Mn^{4+}/Mn^{3+} couple, along with suppressed redox activity of Mn^{3+}/Mn^{2+} couple that restricts the side reactions. The active particle size, electrode structure and electrolyte conditions could be identified as the key factors that contribute to the performance optimization. The electrode simultaneously and unprecedentedly achieves a working voltage of 2.5 V, maximum energy and power densities of 587 Wh·kg$^{-1}_{cathode}$ and 75 kW·kg$^{-1}_{cathode}$ respectively with a 99.5% capacity retention for 500 cycles at 1 A·g^{-1}.

Introduction

Rechargeable batteries are of great interest with tremendous importance for mobile devices, electrical vehicles, telecommunication equipment and photovoltaic integration. [1-4] Owing to the earth-abundant and low cost of sodium (Na) as compared to lithium (Li), Na secondary batteries are envisioned to be a viable alternative to replace the current Li based battery industry. For the future practical consideration, the target of rechargeable Na battery, such as Na ion battery (SIB), is to achieve energy and power densities of >200 Wh·kg^{-1} and >2 kW·kg^{-1} with a working voltage of ~2.5 V over 4,000 cycles. [5] This requires the battery electrode to achieve high energy density, extraordinary rating capability and long-term cyclic stability.

Taking advantage of lower molar weight, transition metal oxides exhibit higher theoretical capacity as compared to their sulfides and selenides counterparts. Particularly, manganese-based compounds have been widely employed as the electrode materials for rechargeable alkali-ion batteries, such as $LiMn_2O_4$, $Li_4Mn_2O_5$, MnO_2 and Mn_3O_4, etc. [6,7] Among them, as a consequence of its abundance, high theoretical capacity, and environmental compatibility, MnO_2 has been well known as the potential electrode materials for Na-ion batteries. [8] Unfortunately, like other manganese-based electrodes, the conventional MnO_2 electrode suffers from severe capacity fade and poor rating capability which

could be mainly ascribed to some common issues: i) Mn^{3+} disproportionation reaction upon cycling as follows (1): [9]

$$2Mn^{3+} \rightarrow Mn^{2+} + Mn^{4+} \qquad (1)$$
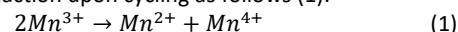
ii) Mn dissolution due to the acid attack which is generated from the decomposition of the solvent. [10] These shortcomings make manganese-based compounds less competitive compared to other recent developing electrode materials. [11,12] Later works turned to MnO_2-based composites, such as graphene/MnO_2 or polymer/MnO_2. [13,14] However, the performance is still unsatisfactory. Despite various mechanisms that caused limited electrochemical performance of MnO_2 electrode have been proposed, an effective approach to overcome the limitations is lacking to date.

In this work, we enhance the cyclic and rating ability of MnO_2 electrode by kinetically controlling the redox behavior. Environmental friendly K-birnessite MnO_2 ($K_{0.3}MnO_2$) nanosheets are prepared *via* a facile approach. To fabricate a SIB, the $K_{0.3}MnO_2$ electrode is prepared by an additive-free inkjet printing system and the diglyme-based electrolyte is selected. Surprisingly, the as-printed $K_{0.3}MnO_2$ electrode shows only one step conversion of Mn^{4+}/Mn^{3+} couple with enhanced redox activity and deteriorating redox activity of Mn^{3+}/Mn^{2+} couple that prevents the occurrence of side reactions, leading to a raised average potential, high power output as well as long term cyclic stability, further serving as a cathode material for high performance SIBs. We reveal that the active particle size, electrode structure and the electrolyte condition could be the key factors that contribute to the performance optimization. This work opens up an avenue to the future development of rechargeable manganese-based alkali-ion batteries through electrode engineering.

Department of Applied Physics, the Hong Kong Polytechnic University, Hong Kong SAR. E-mail: apsplau@polyu.edu.hk

Experimental Section

Synthesis of the $K_{0.3}MnO_2$ nanosheets

All chemicals were analytical reagents that purchased from Sigma-aldrich and used without further purification. The $K_{0.3}MnO_2$ nanosheets were synthesized *via* a modified method according to our previous reports. [15, 16] Typically, 10 wt% glucose solution was poured into Teflon-sealed autoclave (Parr 4748) and heated by hydrothermal treatment at 180 °C for 3 h. When the reaction was completed, the suspension was poured out for filtration. The carbon residues were re-dissolved into distilled (DI) water and sonicated sufficiently to form a 0.1 mg·mL^{-1} carbon suspension. Then 16 mg·mL^{-1} $KMnO_4$ solution was added into the suspension dropwise under continuous stirring and maintained at 45 °C for 8 h. The mass ratio of $KMnO_4$ and carbon was about 8:1. After that the suspension was sealed inside the stainless steel autoclave and heated at 100 °C for 4 h. After cooling to room temperature, the suspension was filtered by using filter membrane (pore size: < 220 nm) to remove the impurities.

Preparation of the R-MnNS electrode

The stainless steel (SS) sheet was thoroughly washed by ethanol and DI water for several times. The suspension was inkjet-printed (PixDro LP50) onto the SS sheet at 40°C to form a conformal layer. After that, the $K_{0.3}MnO_2$ thin films were annealed at 300 °C in air for 2 h. The mass loading was controlled in the range of 0.3 - 0.7 mg·cm^{-2}.

Preparation of the MnNS electrode

The as-prepared $K_{0.3}MnO_2$ nanosheets were dried to obtain powder, and then mixed with carbon black (Super P) and polyvinylidene difluoride (PVDF) in a mass ratio of 7:2:1. The mixture was grinded for 60 min and dispersed in 1-methyl-2-pyrrolidone (NMP) to form slurry. Then the slurry was coated onto the copper foil and drying in vacuum at 60 °C overnight. The mass loading of the active materials was 0.5 - 0.6 mg·cm^{-2}.

Preparation of the K-MnO$_2$ electrode

0.5 g of $KMnO_4$ was mixed with 25 mL ethanol and 25 mL DI water to produce the K-birnessite MnO_2. The mixture was filtered to collect the MnO_2 powder. After that, the MnO_2 powder was annealed at 300 °C in air for 2 h. The as-prepared MnO_2 powder was mixed with carbon black and PVDF in a mass ratio of 6.5:2.5:1. The mixture was grinded for 60 min and dispersed in NMP to form slurry. Then the slurry was coated onto the copper foil and drying in vacuum at 60 °C overnight. The mass loading of the active materials was 0.6 - 0.7 mg·cm^{-2}.

Preparation of the KS6 carbon electrode

KS6 conductive carbon was purchased from MTI, Shenzhen Cor. without further purifications. The KS6 powder was mixed with carbon black and PVDF in a mass ratio of 8:1:1. The mixture was grinded for 60 min and dispersed in NMP to form slurry. Then the slurry was coated onto the copper foil and drying in vacuum at 60 °C overnight. The mass loading of the active materials was ~1.68 mg·cm^{-2}.

Assembly of the coin cell

CR2032 coin cells were assembled in an argon-filled Mbraun glovebox (with both H_2O and O_2 contents less than 0.5 ppm). The $K_{0.3}MnO_2$ electrodes were cut into small circles for battery test. Na metal or KS6 was served as the counter electrode. 1.0 mol·L^{-1} $NaCF_3SO_3$ dissolved in diethylene glycol dimethyl ether (diglyme) was used as the electrolyte.

Materials Characterization

The surface and cross sectional morphologies of the $K_{0.3}MnO_2$ thin films were characterized by scanning electron microscopy (SEM) (Tescan MIMA3). Transmission electron microscopy (TEM) images and select area electron diffraction (SAED) pattern were recorded through a JEM 2100F (field emission) scanning transmission electron microscope (spherical aberration Cs: 2.3mm, Chromatic aberration Cc: 1.0 mm, point resolution 0.23 nm) equipped with an Oxford INCA x-sight EDS Si (Li) detector. XRD pattern was carried out by using a Rigaku SmartLab X-ray diffractometer operating at 45 kV and 200 mA with Cu Kα source (λ=1.54056 Å). Raman spectrum was recorded by using a micro laser Raman spectrometer (DX2, Thermo, λ= 532 nm). Atomic force microscopy (AFM) images were recorded by using Digital Instrumental Nanoscope IV in tapping mode. N_2 adsorption and desorption analysis were measured at -196 °C by using Micromeritics ASAP 2020. X-ray photoelectron spectroscopy (XPS) measurement was carried out using a SKL-12 spectrometer modified with VG CLAM 4 multichannel hemispherical analyzer.

Electrochemical Performance Measurements

The cyclic voltammograms (CV), galvanostatic charge/discharge (GCD), galvanostatic intermittent titration technique (GITT) and rating performance were measured by an Arbin battery test system. The electrochemical impendence spectra (EIS) were carried out on a CHI 660D electrochemical workstation (CH Instruments). An AC stimulus (a sine wave) was applied to the electrochemical cell with amplitude of 5 mV over a frequency range from 10 mHz to 100 kHz. The GITT plots were measured at a current density of 20 mA·g^{-1} for 30 min followed by a resting period of 120 min. The chemical diffusion coefficient of Na^+ ions passing through the R-MnNS electrode can be calculated based on the equation (2):

$$D_{Na^+} = \frac{4}{\pi}\left(\frac{mV_M}{MS}\right)^2 \left(\frac{dE_s/d\delta}{dE_\tau/d\sqrt{\tau}}\right)^2 \approx \frac{4}{\pi\tau}\left(\frac{mV_M}{MS}\right)^2 \left(\frac{\Delta E_s}{\Delta E_\tau}\right)^2 \qquad (2)$$

where m and M are the mass (g) and the molecular weight (g·mol^{-1}) of the active material, respectively. V_M is the molar volume (cm^3·mol^{-1}) of K-birnessite MnO_2, obtainable from the crystallographic information. S is the effective surface area (cm^2) between the active material and the electrolyte and can be considered to be Brunauer-Emmett-Teller (BET) surface area (S_{BET}). $dE_s/d\delta$ is the slope of the coulometric titration curve which can be obtained by plotting the equilibrium electrode voltage measured after each titration step δ. $dE_\tau/d\sqrt{\tau}$ denotes the slope of the linearized region of the potential E_τ during the current pulse of duration time τ (sec).

Fabrication of $K_{0.3}MnO_2$ electrodes
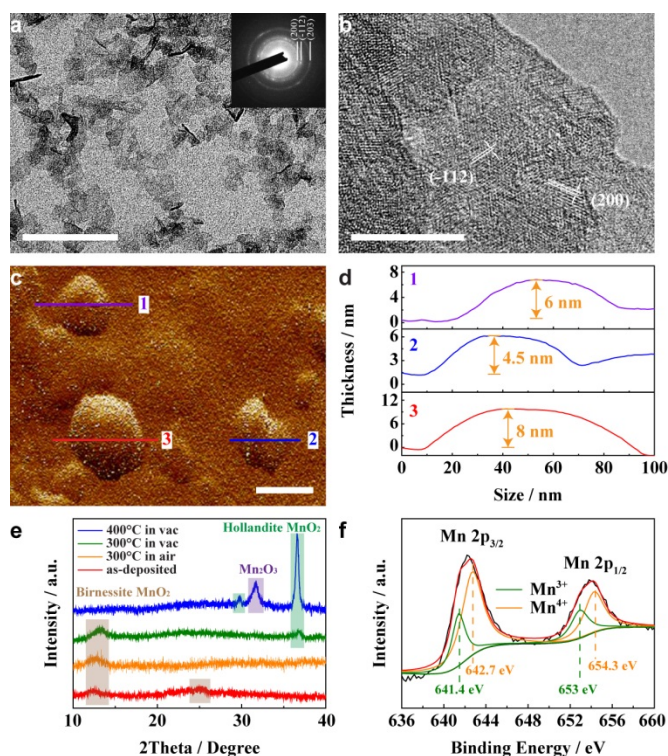
Fig. 1 Characterizations of the $K_{0.3}MnO_2$ nanosheets. a, b) TEM images. Scales bars are 100 nm for panel a and 10 nm for panel b. Inset: the corresponding SAED pattern. c, d) Thickness measurements of the $K_{0.3}MnO_2$ nanosheets by AFM. Scale bar is 50 nm. e) XRD patterns of the $K_{0.3}MnO_2$ nanosheets treated in various conditions. f) XPS spectrum corresponding to the Mn 2p states.

The surface morphologies of the $K_{0.3}MnO_2$ nanosheets are shown in the TEM images of Fig. 1a, b. The average diameter of the $K_{0.3}MnO_2$ nanosheets is estimated to be about 30-70 nm. With reference to JCPDS card No. 80-1098, the selected area electron diffraction (SAED) pattern in the inset of Fig. 1a shows two characteristic diffraction rings at d-spacings of ~2.523, 2.121 and 1.581 Å, which could be attributed to the (200), (-112) and (203) reflections of the $K_{0.3}MnO_2$, respectively. The results can also be confirmed by Raman spectra and energy-dispersive X-ray spectroscopy (EDX) spectrum, as shown in Fig. S1 in the ESI. The absence of diffraction rings of (001) and (002) in the SAED pattern is attributed to the fact that the possibility of the nanosheet surfaces parallel to the electron beam is very low and the corresponding contribution to the SAED pattern cannot be detected. [17] Fig. 1c, d show the thickness measurements of three single $K_{0.3}MnO_2$ nanosheets through the AFM image. Sloping edges of the single $K_{0.3}MnO_2$ nanosheets can be clearly observed in accordance to the results in the TEM images. The thicknesses of the nanosheets are between 4 and 8 nm. Fig. 1e shows the XRD patterns of the $K_{0.3}MnO_2$ nanosheets prepared under different conditions (as-prepared, annealed at 300 °C in vacuum and air and 400 °C in vacuum). The XRD pattern of the MnO_2 nanosheets exhibits two peaks at 12.5° and 25°, which can be assigned to the K-birnessite MnO_2 and also agrees with the SAED results. When the sample annealed at 300 °C in air or vacuum, the diffraction peak at 12.5° can still be observed, while another small peak at 36° corresponding to the formation of hollandite MnO_2 (JCPDS No. 44-0141) can be observed for the sample annealed in vacuum. If the annealing

temperature continues rising to 400 °C, the peaks belong to K-birnessite MnO_2 both disappeared. However, the intensity of hollandite MnO_2 peak becomes much higher and another peak belonged to Mn_2O_3 (JCPDS No. 41-1442) appears at 31°. The $K_{0.3}MnO_2$ nanosheets were coated onto the SS sheet and annealed for 2 h to form a thin film for the XPS analysis. As shown in Fig. 1f, two distinct peaks at 642 and 654 eV could be observed, which could be assigned to the Mn $2p^{1/2}$ and Mn $2p^{3/2}$ peaks, respectively. The Mn 2p spectrum could be divided into two major components corresponding to the existence of Mn^{4+} and Mn^{3+}. To identify the Mn/K ratio, the XPS spectrum corresponding to Mn 3s states is shown in Fig. S2. According to a linear relationship between the oxidation state of manganese and the ΔE value, the energy separation between the two peaks of Mn 3s is 4.87 eV, which corresponds to an average Mn oxidation state of +3.7. [18, 19] The chemical formula could be identified as $K_{0.3}Mn_{0.3}^{3+}Mn_{0.7}^{4+}O_2$ ($K_{0.3}MnO_2$), which is confirmed by the inductive coupled plasma optical emission spectrometry (ICP-OES) analysis.

The $K_{0.3}MnO_2$ nanosheets suspension was poured into the cartridge of an inkjet printing system. As shown in Fig. 2a, the inkjet printing system could eject the droplets (~70 μm in diameter) containing the $K_{0.3}MnO_2$ nanosheets onto the SS sheet at 40 °C without any additives (Fig. S3). The droplets are dried in a very short time, leading to a layer by layer stacking of the $K_{0.3}MnO_2$ nanosheets. The printing speed can be tuned between 150 and 600 $cm \cdot min^{-1}$. The mass loading is adjustable by repeatedly printing. The as-printed $K_{0.3}MnO_2$ electrode is annealed at 300 °C for 2 h to remove the water molecule and improve the crystallinity without phase change according to the results of XRD patterns (Fig. 1e) and previous report. [20] The SEM images of the inkjet-printed $K_{0.3}MnO_2$ electrode (denoted as R-MnNS electrode) shows a conformal and porous structure. High-resolution SEM and TEM images shown in Fig. S4 reveal that the diameter of the pores are ranging from 10 to 100 nm, which could be further confirmed by the results of BET surface area and pore size distribution analysis (Fig. S5). Taking advantages of the nano-structured $K_{0.3}MnO_2$, the hierarchical porous structure could accommodate the possible volume expansion and facilitate the Na^+ ions transportation on the interface between the electrode and electrolyte. [21, 22] In contrast, the traditional slurry-coating method is briefly illustrated and employed for battery electrode production, as shown in Fig. 2b. The $K_{0.3}MnO_2$ nanosheets were collected after annealing at 300 °C in air for 2 h. The $K_{0.3}MnO_2$ powder were mixed with the carbon black (CB) and PVDF (mass ratio (MnO_2:CB:PVDF) = 7:2:1), then deposited onto the Cu foil to form the electrode (denoted as MnNS electrode) through roll-to-roll slurry coating. Owing to the introduction of additives during the extra slurry formation steps, particle-like aggregates of the $K_{0.3}MnO_2$/CB/PVDF ternary mixture with >50 nm in diameter formed a loose structure.

Redox behaviors of the $K_{0.3}MnO_2$ electrodes

Coin cells were firstly assembled by using different MnO_2 electrodes as the working electrode and Na metal as the counter electrode with diglyme or carbonate-based electrolyte in between. As the reference of bulk materials, the K-birnessite MnO_2 aggregated from several hundred sub-micrometers to several

ARTICLE Journal Name
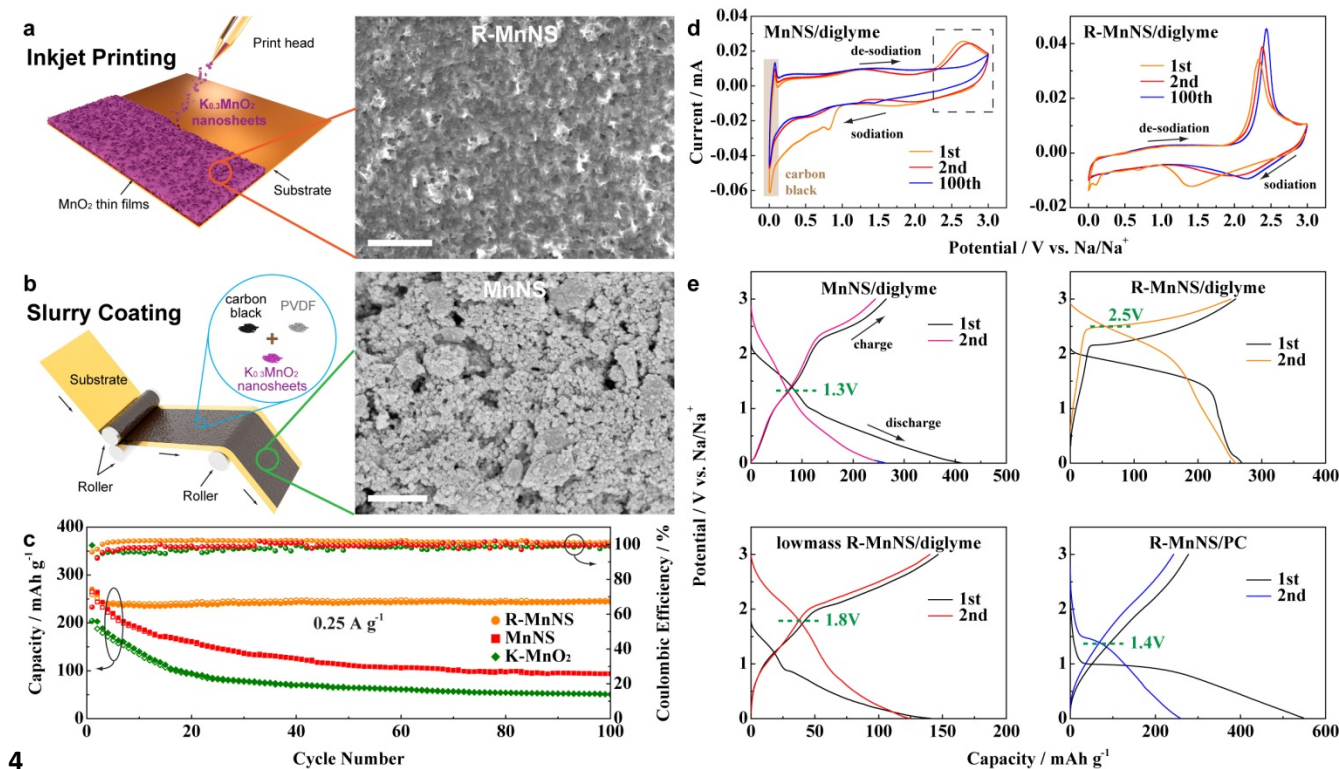
Fig. 2 Redox behaviors of the MnNS and R-MnNS electrodes. a, b) Schematic diagrams of the inkjet printing and slurry coating processes and the corresponding SEM images of the as-prepared $K_{0.3}MnO_2$ electrodes. Scale bars are 2 μm for panel a and 1 μm for panel b. c) Cyclic performance and coulombic efficiencies of different MnO_2 electrodes for 100 cycles at 0.25 A·g^{-1}. d) 1st, 2nd and 100th CV profiles of the MnNS (left) and R-MnNS (right) electrodes at 0.1 mV·s^{-1}. e) 1st and 2nd GCD profiles of MnNS and R-MnNS electrodes with different mass loading and electrolyte conditions at 0.25 A·g^{-1}.

micrometers in diameter were prepared and served as the active materials of the battery electrode *via* traditional slurry-coating process (denoted as K-MnO$_2$ electrode), as shown in Fig. S6. The reversible capacities and coulombic efficiencies profiles at 0.25 A·g^{-1} are shown in Fig. 2c. All the three electrodes show ~100% coulombic efficiencies after 3 cycles. Both the MnNS and K-MnO$_2$ electrodes show heavy irreversible capacity of ~40% in the first cycle. The cycling profile of the MnNS electrode shows a limited enhanced reversible capacity of ~40 mAh·g^{-1} compared to that of the K-MnO$_2$ electrode. But both electrodes exhibit similar trends with rapid capacity decays to <150 mAh·g^{-1} for the first 20 cycles and remain ca. 100 mAh·g^{-1} after 100 cycles. In contrast, the discharge capacity of the R-MnNS electrode could reach ca. 270 mAh·g^{-1} for the first cycle and exhibits a straight horizontal line after slightly capacity decay (~10% irreversible capacity) after the first 3 cycles, indicating only less amount of electrolyte could be decomposed during the SEI formation. The discharge capacity of R-MnNS electrode remains ca. 236 mAh·g^{-1} (~87% capacity retention) after 100 cycles, demonstrating a significantly enhanced cyclic stability compared to the MnNS and K-MnO$_2$ electrodes. Besides, the influence of substrate has been investigated, as shown in Fig. S7. The GCD profiles of MnNS electrodes on Cu foil and SS sheet show both anode-like redox behaviors, which could be similar to each other.

To investigate the origin of capacity loss, the CV profiles of the MnNS and R-MnNS electrodes in diglyme-based electrolyte (denoted as MnNS/diglyme and R-MnNS/diglyme) are shown in Fig. 2d. The first discharge cycle of the MnNS/diglyme system shows

two slopes at 1.8 and 0.8 V, which can be attributed to the solid-electrolyte interphase (SEI) formation and the two-step reduction reaction involving $Mn^{4+}/Mn^{3+}/Mn^{2+}$. [23, 24] The slopes move to 2 and 1.2 V from the second discharge cycle. Another couple of redox peaks located at 0.01 V of discharge state and 0.06 V of charge state could be observed, which should be ascribed to the insertion/extraction reactions between Na$^+$ ions and carbon black. [25] During the charging process, two oxidation peaks appeared at 1.25 and 2.6 V, demonstrating a two-step oxidation involving Mn^{3+}/Mn^{2+} and Mn^{4+}/Mn^{3+} couples, respectively. However, the Mn^{4+}/Mn^{3+} conversion (in black dash line) entirely disappears after 100 cycles, which could be hindered by the disproportionation reaction of Mn^{3+}. On the other hand, the first cycle of the R-MnNS/diglyme system shows only one couple of redox peaks except the peak at ~0.15 V due to the SEI formation process. Compared to the MnNS/diglyme system, a larger voltage plateau located at 2 - 1.5 V of discharge state can be seen, revealing a kinetically enhancement of the Mn^{4+}/Mn^{3+} couple. The plateau moves to ~2.2 V in the second discharge cycle due to a low over-potential. When charging, a plateau at 2.1 V could be observed which moves to ~2.4 V in the second charge cycle, again indicating the main capacity contribution of R-MnNS electrode comes from the enhanced reactivity of Mn^{4+}/Mn^{3+} couple. No peak could be observed when the voltage decreases below 1.5 V in the second cycle, indicating a limited redox activity of the Mn^{3+}/Mn^{2+} couple. Furthermore, the 100th CV profile of R-MnNS/diglyme system remains almost unchanged compared to the 2nd one, implying the side reactions are suppressed. To further elucidate the redox
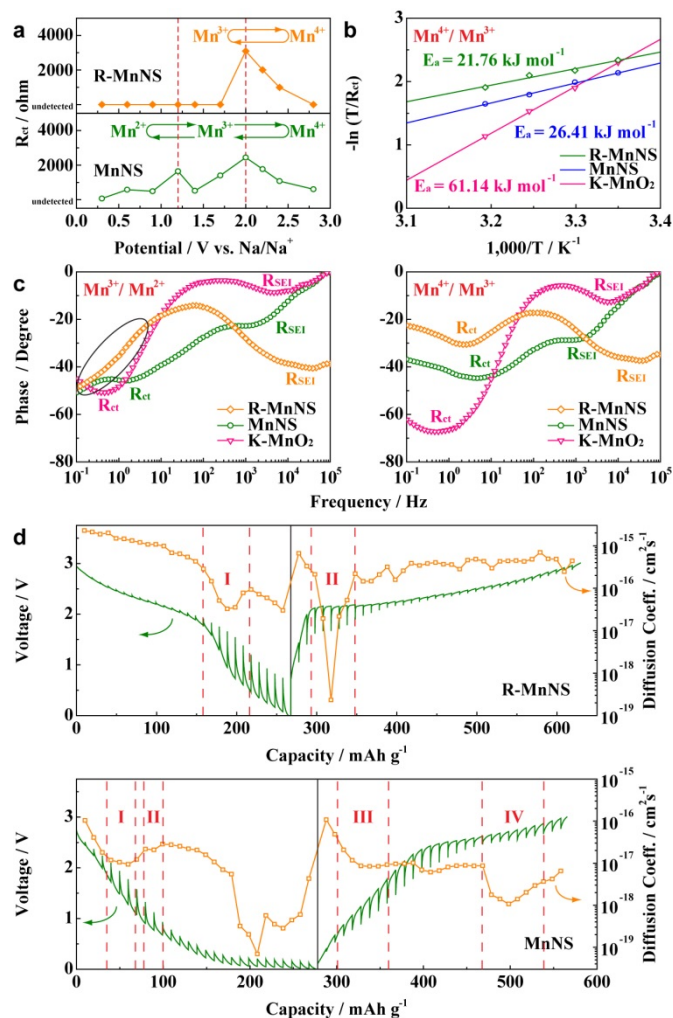
Fig. 3 Kinetics investigations. a) R_{ct} versus voltage plots of the MnNS and R-MnNS electrodes. b) Arrhenius plots of -ln(T/R_{ct}) versus 1,000/T of the Mn^{4+}/Mn^{3+} couple for the K-MnO$_2$, MnNS and R-MnNS electrodes. c) Phase versus frequency plots of Mn^{3+}/Mn^{2+} (left) and Mn^{4+}/Mn^{3+} (right) couples for the K-MnO$_2$, MnNS and R-MnNS electrodes. d) GITT plots of the R-MnNS (top) and MnNS (bottom) electrodes at 20 mA·g^{-1} and corresponding diffusion coefficient of Na$^+$ ions.

behaviors, the 1st and 2nd GCD profiles of MnNS and R-MnNS electrodes with different mass loading and electrolyte conditions at 0.25 A·g^{-1} are shown in Fig. 2e. The GCD profiles of the MnNS/diglyme and R-MnNS/diglyme systems are consistent with the results of the CV profiles. Due to the enhanced activity of Mn^{4+}/Mn^{3+} couple and suppressed redox activity of Mn^{3+}/Mn^{2+} couple, the average potential of R-MnNS/diglyme system increases to ~2.5 V, leading to a potential to serve as the cathode materials. Interestingly, the R-MnNS electrode with low mass loading (0.06 mg·cm^{-2}; mass of active materials = 0.15 mg; thickness = ~1 μm) in diglyme-based electrolyte (lowmass R-MnNS/diglyme) shows a transitional state with partially enhanced Mn^{4+}/Mn^{3+} couple but partially limited Mn^{3+}/Mn^{2+} couple as compared to the MnNS/diglyme and R-MnNS/diglyme. Besides, the R-MnNS electrode in propylene carbonate (PC) based electrolyte (R-MnNS/PC) also shows an anode-like behavior with an average potential of 1.4 V. As noted previously, the difference in ion dissociating ability between diglyme and carbonate based
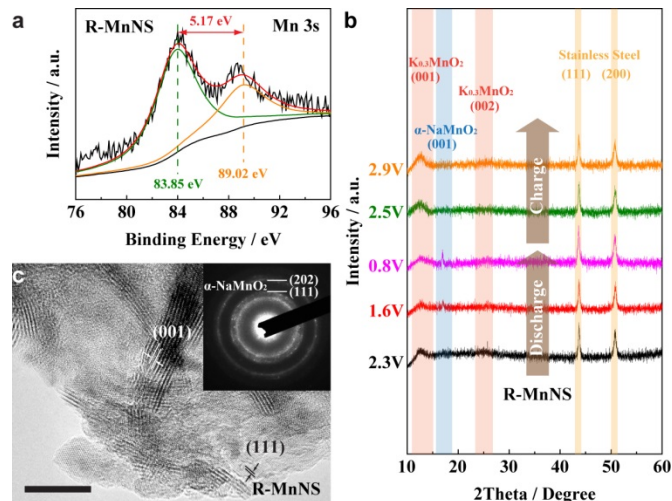
Fig. 4 Phase transformation analysis. a) XPS spectrum corresponding to the Mn 3s state of the fully discharged electrode. b) *Ex-situ* XRD patterns at different states. c) TEM image of the electrode at the charge state of 0.8 V. Scale bar is 10 nm. Inset: the corresponding SAED pattern.

electrolytes may lead to a different kinetic barrier. [12] In our case, one plateau could be observed at 1 V in the first discharge cycle that moves to 1.5 V in the second discharge cycle, revealing the electrolyte could be one of the key factors to change the redox behavior. As shown in Fig. S8, the *in-situ* height profiles of the R-MnNS electrode at 2 and 0 V of discharge state in the second cycle both show a similar surface morphology and height difference as compared to the original one, indicating a highly structural stability of the R- MnNS electrode.

## Kinetics investigation of K$_{0.3}$MnO$_2$ electrodes

For an in-depth understanding of the kinetics of R-MnNS/diglyme system, EIS spectra of MnNS, R-MnNS and K-MnO$_2$ electrodes in diglyme-based electrolyte at different temperatures and voltages have been measured, as shown in Fig. S9 and S10. The charge transfer resistance (R_{ct}) value of the MnNS electrode shows two peaks at 2.0 and 1.2 V of the discharge state (Table S1), which corresponds to the Mn^{4+}/Mn^{3+} and Mn^{3+}/Mn^{2+} couples, respectively. In contrast, only one maximum R_{ct} values is detected from the R-MnNS electrode at 2.0 V of discharge state, implying a fully suppression of Mn^{3+}/Mn^{2+} couple that may avoid the manganese disproportionation and dissolution, as shown in Fig. 3a. Based on the R_{ct} change at different temperatures (Fig. S10), the apparent activation energy (E_a) values of Mn^{4+}/Mn^{3+} couple of K-MnO$_2$, MnNS and R-MnNS electrodes could be calculated according to the following equations (3, 4):

$$i_0 = Ae^{-\frac{E_a}{RT}} \tag{3}$$
$$i_0 = \frac{RT}{nFR_{ct}} \tag{4}$$

where i_0 is the exchange current, A is the temperature-independent coefficient, R is the gas constant, T is the absolute temperature, n is the number of transferred electrons, F is the Faraday constant. Due to the nano-structuring of active materials, the E_a value of the MnNS electrode (26.41 kJ·mol^{-1}) is much lower than that of the K-MnO$_2$ electrode (61.14 kJ·mol^{-1}), as shown in Fig. 3b. Making use of the homogeneous and unique electrode structure, the E_a value of
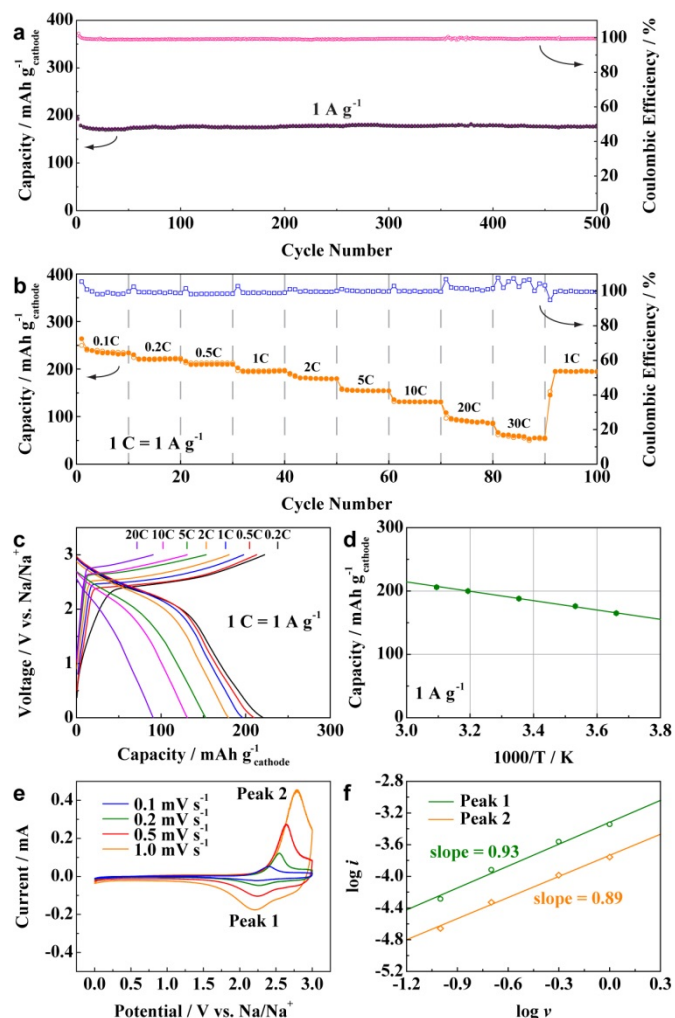
Fig. 5 Electrochemical performance of the R-MnNS electrode. a) Long term cyclic performance and coulombic efficiency for 500 cycles at 1 A·g⁻¹. b) Rate capability and coulombic efficiency at the current densities of 0.1 - 30 A·g⁻¹. c) GCD profiles at different current densities of 0.2 - 20 A·g⁻¹. d) Reversible capacity as a function of temperature from 273 K to 313 K. e, f) CV profiles at different scan rates (e) and the corresponding log(*i*, current) versus log(*v*, scan rate) plots (f) at different redox states.

the R-MnNS electrode reaches 21.76 kJ·mol⁻¹, even lower than that of the MnNS electrode, leading to an enhanced redox activity of Mn^{4+}/Mn^{3+} couple. The phase versus frequency plots obtained from EIS plots of both Mn^{3+}/Mn^{2+} and Mn^{4+}/Mn^{3+} couples for the K-MnO_2, MnNS and R-MnNS electrodes are shown in Fig. 3c. Two semi-circles can be observed from the curves of the K-MnO₂ and MnNS electrodes during two redox conversions, from which the electron lifetime (τ) of the K-MnO₂ electrode could be calculated as 1.8 and 2.13 s upon the Mn^{4+}/Mn^{3+} and Mn^{3+}/Mn^{2+} conversions,[30] while the τ values of MnNS electrode could be only 0.18 and 0.58 s, respectively, again demonstrating the enhancement of redox activity after $K_{0.3}MnO_2$ nano-structuring. Only one semi-circle belonged to Mn^{4+}/Mn^{3+} couple could be observed from the EIS plots of R-MnNS electrode. The τ value could be calculated as 0.41 s, which is on the same level as compared to MnNS electrode even without carbon. The diffusion coefficient of Na⁺ ions was determined by the GITT measurements, as shown in Fig. 4d. Both shapes of GITT curves of the MnNS and R-MnNS electrodes are very
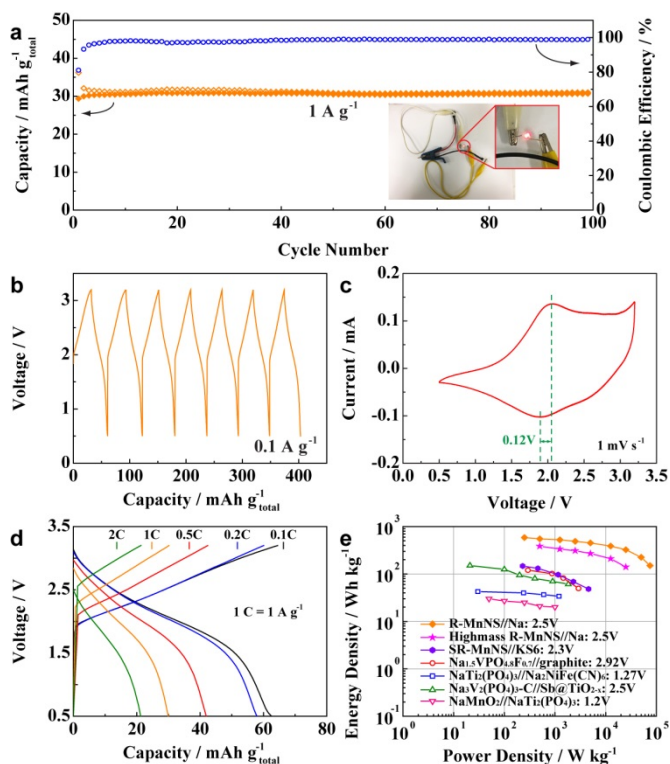
Fig. 6 Electrochemical performance of the SR-MnNS//KS6 full cell. a) Cyclic performance and coulombic efficiency for 100 cycles at 1 A·g⁻¹. Inset: Photograph of a red LED lighted up by a single SR-MnNS//KS6 cell. b) GCD cycles at 0.1 A·g⁻¹. c) CV profile in the voltage range of 0.5 - 3.2 V at 1 mV·s⁻¹. d) GCD profiles at different current densities of 0.1 - 2 A·g⁻¹. e) Energy and power densities of the R-MnNS//Na: 2.5 V, Highmass R-MnNS//Na: 2.5V and SR-MnNS//KS6: 2.3 V compared with $Na_{1.5}VPO_{4.8}F_{0.7}$//graphite: 2.92 V (ref. 35), $NaTi_2(PO_4)_3$//$Na_2NiFe(CN)_6$: 1.27 V (ref. 36), $Na_3V_2(PO_4)_3$-C//Sb@TiO₂₋ₓ: 2.5 V (ref. 37) and $NaMnO_2$//$NaTi_2(PO_4)_3$: 1.2 V (ref. 38).

similar to the charge/discharge curves in Fig. 2e, indicating the electrodes are close to the equilibrium during charging/discharging.[31] The Na⁺ ions diffusion coefficient values of the R-MnNS electrode are mainly in the order of 10^{-16} cm²·s⁻¹ except for the two minimum values in region I and II which could be attributed to the Mn^{4+}/Mn^{3+} couple. In contrast, four minimum values in region I to IV corresponding to the two-step anode behavior could be found from the GITT plots of MnNS electrode, which also agrees with the results of the differential capacitance plots. (Fig. S11)

Phase transformation of $K_{0.3}MnO_2$ electrodes

The XPS analysis of the fully discharged R-MnNS electrode was performed. As shown in Fig. 4a, the Mn 3s spectrum of the fully discharged R-MnNS electrode exhibits a *ΔE* value of 5.17 eV, which corresponds to the average Mn oxidation state of ~3.25. The value indicates that the charge storage mainly originates from the redox conversion involving Mn^{4+}/Mn^{3+} couple. To confirm the intermediate species upon the charge/discharge process, the *ex-situ* XRD patterns of the R-MnNS electrode at different voltages were measured, as shown in Fig. 4b. Except the peaks belonged to the (001) and (002) reflections of $K_{0.3}MnO_2$ at 12.5° and 25°, an unknown peak appeared at ~16.7° was recorded by the XRD patterns at discharge state of 1.6 V and charge state of 0.8 V, which is attributed to the formation of intermediate species triggered by

Table 1 Comparison of the performance between the R-MnNS based and other sodium-ion batteries.

Ref.	Configuration (cathode//anode)	Voltage / V	Capacity Retention / % (cycles)	Energy Density / Wh·kg^{-1}	Power Density / W·kg^{-1}
35	Na$_{1.5}$VPO$_{4.8}$F$_{0.7}$//graphite[c]	2.92	70% (250)	120	---
39	FeS$_2$//Na[b]	~2	>95% (5)	~400	---
40	Na$_{0.8}$Li$_{0.12}$Ni$_{0.22}$Mn$_{0.66}$O$_2$// Sn@CNT-CP[c]	3.1	50% (40)	---	---
21	Se-CCN//PGC[c]	1.5	76% (150)	203	14,000
41	Na$_{2-\delta}$MnHFC//hard carbon[b]	3.3	>90% (30)	180	900
42	NaNi$_{0.5}$Mn$_{0.5}$O$_2$//hard carbon[b]	3	52% (80)	---	---
43	Na$_2$Ti$_3$O$_7$//VOPO$_4$[b]	3.2	92.4% (100)	220	1,500
36	NaTi$_2$(PO$_4$)$_3$//Na$_2$NiFe(CN)$_6$[c]	1.27	88% (250)	42.5	1,200
37	Na$_3$V$_2$(PO$_4$)$_3$-C//Sb@TiO$_{2-x}$[c]	2.5	~70% (100)	151	1,830
38	NaMnO$_2$//NaTi$_2$(PO$_4$)$_3$[c]	1.2	75% (500)	30	1,000
This work	**R-MnNS (~0.75 mg)//Na[b]**	**2.5**	**91% (500)**	**587**	**75,000**
	R-MnNS (~1.41 mg)//Na[b]	**2.5**	**---**	**385**	**25,000**
	SR-MnNS (~0.75 mg)//KS6[c]	**2.3**	**~100% (100)**	**147**	**4,600**

Note: [a] – the value is calculated based on the mass of the anode materials; [b] – the value is calculated based on the mass of the cathode materials; [c] – the value is calculated based on the total mass of the electro-active materials.

the Mn^{4+}/Mn^{3+} conversion. The location of the characteristic peak matches closely to the (001) reflection of α-NaMnO$_2$ according to the previous report and the JCPDS card (No. 72-0830), [27, 28] which could be further identified by the SAED pattern of the R-MnNS electrode at charge state of 0.8 V in Fig. 4c. To further confirm the intermediate phase, the GCD profile of the R-MnNS electrode was also tested in the potential range of 1.5 - 3.5 V, which could be similar to the GCD profile of α-NaMnO$_2$, [29] as shown in Fig. S12. Based on the confirmed intermediate phase, the theoretical capacity of the R-MnNS electrode can be calculated as 272 mAh·g^{-1}.

Proposed mechanism

Compared to the MnNS and K-MnO$_2$ electrodes, the R-MnNS electrode shows exceptional redox behavior with raised average potential, enhanced rating capability and prolonged cyclic life. Such an improved performance could be attributed to four points: i) based on the comparison of reversible capacity, the nano-structured K$_{0.3}$MnO$_2$ enhances the redox activity of Mn^{4+}/Mn^{3+} couple; ii) the comparison of R-MnNS/diglyme and R-MnNS/PC systems in the control experiment indicate the usage of diglyme-based electrolyte may reduce the irreversible capacity; iii) the surface morphology images show a porous structure that allows a rapid Na$^+$ ions transportation; vi) according to the kinetics investigation and phase transformation analysis, the electrode structure increases the E_a value to dramatically reduce the redox activity of Mn^{3+}/Mn^{2+} couple, leading to a fully suppression of manganese dissolution and Mn^{3+} disproportionation reaction.

Half cell and full cell performance

The R-MnNS based half cell was further tested to evaluate the performance. As shown in Fig. 5a, the reversible capacity of the R-MnNS electrode can still maintain 142 mAh·g$^{-1}_{cathode}$ (91% capacity retention) at 1 A·g^{-1} after 500 cycles, indicating a long term cycling capability. As shown in Fig. 5b and 5c, with the increase of current densities from 0.1, 0.2, 0.5, 1, 2, 5 to 10 A·g^{-1}, the average capacities

of R-MnNS electrode (calculated based on the cathode mass) could reach 235, 220, 210, 195, 180, 155 and 130 mAh·g$^{-1}_{cathode}$, respectively. Even if increasing the current density to ultrahigh value of 30 A·g^{-1}, the discharge capacity of the cell could still maintain 60 mAh·g$^{-1}_{cathode}$, revealing a potential for high power devices. [32] By returning to the initial current density of 1 A·g^{-1}, the reversible capacity is fully recovered. As shown in Fig. S13, if one R-MnNS electrode with high mass loading of 0.7 mg·cm^{-2} (cathode mass: 1.41 mg) is applied, the reversible capacity can remain at ~155 mAh·g$^{-1}_{cathode}$ at 0.2 A·g^{-1} with a similar GCD profiles (cathode mass = ~0.75 mg) compared to the results in Fig. 2e. To further increase the mass loading of the active materials, we believe a designed electrode structure is required, such as layer-by-layer, which could be the subject of another publication in the future. The CV profiles at different scan rates are shown in Fig. 5e. When the scan rate increases, the peak current increases without being proportional to the square root of the scan rate, which illustrates that the charge and discharge processes are composed of non-Faradaic and Faradaic behaviors. [33, 34] The relationship between peak current (i) and scan rate (v) can be described by the equations as follows (5):

$$\log(i) = b\log(v) + \log(a) \tag{5}$$

where i is the peak current, v is the scan rate, and a and b are the adjustable parameters. The b value determines the type of Na$^+$ insertion/extraction. If the b value is close to 0.5, the electrochemical reaction is controlled by ionic diffusion; and if b value is close to 1, the process mainly relies on pseudo-capacitive control. Fig. 5f presents the linear relationship between log(i) and log(v) plots at every peak potential. The b values of the two redox peaks are 0.93 and 0.89, which implies that the redox conversions are mainly attributed to the pseudo-capacitive contribution, leading to a high-rate performance. After the measurements for five times, the discharge capacities of the R-MnNS electrode at different current densities with deviation of no more than 20% are achieved. Besides, the coulombic efficiency of the R-MnNS electrode can reach ~100% from the first cycle and remains 99.46% after 500 cycles at 1 A·g^{-1}. As shown in Fig. 5d, the discharge capacity of the

ARTICLE Journal Name

R-MnNS electrode could maintain in the range of 132 - 164 mAh·g$^{-1}_{cathode}$ at 1 A·g^{-1} when the temperature varies from 273.15 to 313.15 K, indicating the stable cyclic performance of the R-MnNS electrode at room temperature. Furthermore, the R-MnNS electrode can achieve a reversible capacity of ca. 110 mAh·g$^{-1}_{cathode}$ after 200 cycles at 1 A·g^{-1} in the gelled diglyme-based electrolyte, as shown in Fig. S14.

To demonstrate the potential of R-MnNS electrode to serve as cathode materials for SIBs, a full cell was fabricated by using pre-sodiated R-MnNS cathode and KS6 carbon anode based on the half-cell specific capacity values (denoted as SR-MnNS//KS6 cell), and then tested in the NaCF$_3$SO$_3$/digylme electrolyte with a voltage range of 0.5 - 3.2 V. The cyclic performance of KS6 carbon electrode is shown in Fig. S15. A discharge capacity of ca. 116 mAh·g$^{-1}_{anode}$ could be reached with a highly cyclic stability for 20 cycles. An obvious discharge plateau could be observed at ~0.6 V. As shown in Fig. 6a, the discharge capacity of the SR-MnNS//KS6 cell (calculated by the total mass of cathode and anode) can maintain at 30 mAh·g$^{-1}_{total}$ (~100% capacity retention) at a high current density of 1 A·g^{-1}, along with > 98% coulombic efficiency over 100 cycles. Notably, the high capacity retention could be much better than other recent reported SIBs, as listed in Table 1. To demonstrate the practical usage of the full cell, a red light-emitting diode (LED) can be lighted up by a single SR-MnNS//KS6 cell. GCD cycles at a current density of 0.1 A·g^{-1} (Fig. 6b) demonstrate the high cyclic stability of the full cell, which is consistent of the results of the capacity test. The CV profile at 1 mV·s^{-1} is shown in Fig. 6c. Two well-defined peaks could be observed at 2.02 V of charge state and 1.9 V of discharge state, which is consistent with the voltage difference between R-MnNS cathode and KS6 anode. A low potential hysteresis of 0.12 V could be calculated, which agrees with the rating performance in Fig. S16. As shown in Fig. 6d, the SR-MnNS//KS6 cell achieves rating capacities (calculated based on the total mass including cathode and anode) of 64, 57, 42, 30 and 21 mAh·g$^{-1}_{total}$ when the current density increases from 0.1 to 2 A·g^{-1}. Besides, the average working voltage of the SR-MnNS//KS6 cell could be kept at ~2.3 V. Fig. 6e shows the energy and power densities (Ragone plots) for a comprehensive comparison between the R-MnNS based and other recent-reported sodium-ion batteries. If only the cathode mass is calculated, the values of energy and power densities of the R-MnNS electrode can reach up to 587 Wh·kg$^{-1}_{cathode}$ and 75 kW·kg$^{-1}_{cathode}$, respectively. If the R-MnNS electrode with mass loading of 0.7 mg·cm^{-2} is applied, the energy and power densities could still remain at 385 Wh·kg$^{-1}_{cathode}$ and 25 kW·kg$^{-1}_{cathode}$, respectively. When the total mass including cathode and anode is calculated, the SR-MnNS//KS6 full cell could reach an average working voltage of 2.3 V with maximum energy and power densities of 147 Wh·kg$^{-1}_{total}$ and 4.6 kW·kg$^{-1}_{total}$, respectively. The cell simultaneously achieves ideal working voltage, energy and power output as well as high capacity retention as compared to other SIBs [20, 35-38], even approaching the target for future SIBs (200 Wh·kg$^{-1}_{total}$ and 2 kW·kg$^{-1}_{total}$).

Conclusions

In summary, to address the capacity fading issue of manganese-based electrodes caused by Mn^{3+} disproportionation

reaction and manganese dissolution, environmental friendly K$_{0.3}$MnO$_2$ nanosheets and diglyme-based electrolyte were used to fabricate a SIB. In big contrast to the anode-behaved conventional K-MnO$_2$ electrode, the inkjet-printed K$_{0.3}$MnO$_2$ electrode shows only one step conversion of Mn^{4+}/Mn^{3+} couple with enhanced redox activity, which entirely prevents the side reactions and allows it to serve as a cathode material for high performance rechargeable sodium batteries. The average particle size, electrode structure and electrolyte conditions could be the key factors to influence the performance. The as-assembled full cell could reach maximum energy and power densities of 147 Wh·kg$^{-1}_{total}$ and 4.6 kW·kg$^{-1}_{total}$ with an average working voltage of 2.3 V and ca. 100% capacity retention after 100 cycles, which could be anticipated for the practical energy applications. Our findings open up an avenue for the further development and commercialization of manganese compounds-based alkali-ion battery. We envision its use to compete with a targeted future sodium-ion battery.

Conflicts of interest

There are no conflicts to declare.

Acknowledgements

Notes and references

1 J. A. Rogers, T. Someya and Y. Huang, *Science,* 2010, **327**, 1603-1607.
2 J. B. Goodenough and K.-S. Park, *J. Am. Chem. Soc.,* 2013, **135**, 1167-1176.
3 B. Wang, X. Li, X. Zhang, B. Luo, M. Jin, M. Liang, S. A. Dayeh, S. T. Picraux and L. Zhi, *ACS Nano,* 2013, **7**, 1437-1445.
4 Y. Sun, N. Liu and Y. Cui, *Nat. Energy,* 2016, **1**, 16071.
5 L. Peng, Y. Zhu, D. Chen, R. S. Ruoff and G. Yu, *Adv. Energy Mater.,* 2016, **6**, 1600025.
6 X. Xiang, K. Zhang and J. Chen, *Adv. Mater.,* 2015, **27**, 5343-5364.
7 H. Kang, Y. Liu, K. Cao, Y. Zhao, L. Jiao, Y. Wang and H. Yuan, *J. Mater. Chem. A,* 2015, **3**, 17899-17913.
8 D. Su, H.-J. Ahn and G. Wang, *J. Mater. Chem. A,* 2013, **1**, 4845-4850.
9 S. T. Myung, K. Hosoya, S. Komaba, H. Yashiro, Y. K. Sun and N. Kumagai, *Electrochim. Acta,* 2006, **51**, 5912-5919.
10 Y. Dai, L. Cai and R. E. White, *J. Electrochem. Soc.,* 2013, **160**, A182-A190.
11 K. Zhang, Z. Hu, X. Liu, Z. Tao and J. Chen, *Adv. Mater.,* 2015, **27**, 3305-3309.
12 M. Lee, J. Hong, J. Lopez, Y. Sun, D. Feng, K. Lim, W. C. Chueh, M. F. Toney, Y. Cui and Z. Bao, *Nat. Energy,* 2017, **2**, 861-868.
13 C. Guo, M. Wang, T. Chen, X. Lou and C. Li, *Adv. Energy Mater.,* 2011, **1**, 736-741.
14 L. Li, A.-R. O. Raji and J. M. Tours, *Adv. Mater.,* 2013, **25**, 6298-6302.

15   J. Qian, H. Jin, B. Chen, M. Lin, W. Lu, W. M. Tang, W. Xiong, L. W. H. Chan, S. P. Lau and J. Yuan, *Angew. Chem. Int. Ed.,* 2015, **54**, 6800-6803.
16   H. Jin, J. Qian, L. Zhou, J. Yuan, H. Huang, Y. Wang, W. M. Tang and L. W. H. Chan, *ACS Appl. Mater. Interfaces,* 2016, **8**, 9088-9096.
17   T. T. Truong, Y. Liu, Y. Ren, L. Trahey and Y. Sun, *ACS Nano,* 2012, **6**, 8067-8077.
18   X.-F. Lu, Z.-X. Huang, Y.-X. Tong and G.-R. Li, *Chem. Sci.,* 2016, **7**, 510-517.
19   M. Nakayama, S. Konishi, H. Tagashira and K. Ogura, *Langmuir,* 2005, **21**, 354-359.
20   R. Chen, P. Zavalij and M. S. Whittingham, *Chem. Mater.,* 1996, **8**, 1275-1280.
21   J. Ding, H. Zhou, H. Zhang, T. Stephenson, Z. Li, D. Karpuzov and D. Mitlin, *Energy Environ. Sci.,* 2017, **10**, 153-165.
22   L. Peng, P. Xiong, L. Ma, Y. Yuan, Y. Zhu, D. Chen, X. Luo, J. Lu, K. Amine and G. Yu, *Nat. Commun.,* 2017, **8**, 15139.
23   A. Yu, H. W. Park, A. Davies, D. C. Higgins, Z. Chen and X. Xiao, *J. Phys. Chem. Lett.,* 2011, **2**, 1855-1860.
24   Z. Zhang, X. Zhao and J. Li, *ChemNanoMat,* 2016, **2**, 196-200.
25   L. Wang, K. Zhang, Z. Hu, W. Duan, F. Cheng and J. Chen, *Nano Res.,* 2014, **7,** 199-208.
26   H. Bock, C. Naether and Z. Havlas, *J. Am. Chem. Soc.,* 1995, **117**, 3869-3870.
27   A. M. Abakumov, A. A. Tsirlin, I. Bakaimi, G. V. Tendeloo and A. Lappas, *Chem. Mater.,* 2014, **26**, 3306-3315.
28   Y. Li, X. Feng, S. Cui, Q. Shi, L. Mi and W. Chen, *CrystEngComm,* 2016, **18**, 3136-3141.
29   X. Ma, H. Chen and G. Ceder, *J. Electrochem. Soc.,* 2011, **158**, A1307-A1312.
30   J. Halme, P. Vahermaa, K. Miettunen and P. Lund, *Adv. Mater.,* 2010, **22**, E210-E234.
31   S. Yuan, X. Huang, D. Ma, H. Wang, F. Meng and X. Zhang, *Adv. Mater.,* 2014, **26**, 2273-2279.
32   A. Varzi, D. Bresser, J. Zamory, F. Müller and S. Passerini, *Adv. Energy Mater.,* 2014, **4**, 1400054.
33   J. Wang, J. Polleux, J. Lim and B. Dunn, *J. Phys. Chem. C,* 2007, **111**, 14925-14931.
34   L. Yu, L. Zhang, H. Wu and X. Lou, *Angew. Chem. Int. Ed.,* 2014, **53**, 3711-3714.
35   H. Kim, J. Hong, Y.-U. Park, J. Kim, I. Hwang and K. Kang, *Adv. Funct. Mater.,* 2015, **25**, 534-541.
36   X. Wu, Y. Cao, X. Ai, J. Qian and H. Yang, *Electrochem. Commun.,* 2013, **31**, 145-148.
37   N. Wang, Z. Bai, Y. Qian and J. Yang, *Adv. Mater.,* 2016, **28**, 4126-4133.
38   Z. Hou, X. Li, J. Liang, Y. Zhu and Y. Qian, *J. Mater. Chem. A,* 2015, **3**, 1400-1404.
39   A. P. Cohn, N. Muralidharan, R. Carter, K. Share and C. L. Pint, *Nano Lett.,* 2017, **17**, 1296-1301.
40   X. Xie, K. Kretschmer, J. Zhang, B. Sun, D. Su and G. Wang, *Nano Energy,* 2015, **13**, 208-217.
41   J. Song, L. Wang, Y. Liu, J. Liu, B. Guo, P. Xiao, J.-J. Lee, X. Yang, G. Henkelman and J. B. Goodenough, *J. Am. Chem. Soc.,* 2015, **137**, 2658-2664.
42   S. Komaba, W. Murata, T. Ishikawa, N. Yabuuchi, T. Ozeki, T. Nakayama, A. Ogata, K. Gotoh and K. Fujiwara, *Adv. Funct. Mater.,* 2011, **21**, 3859-3867.
43   H. Li, L. Peng, Y. Zhu, D. Chen, X. Zhang and G. Yu, *Energy Environ. Sci.,* 2016, **9**, 3399-3405.